Absolute cross section measurements for the scattering of low- and intermediate-energy electrons from PF_3. II. Inelastic scattering of vibrational and electronic excitations

N. Hishiyama, M. Hoshino, F. Blanco, G. García, and H. Tanaka

Citation: The Journal of Chemical Physics **148**, 084313 (2018); doi: 10.1063/1.5012844
View online: https://doi.org/10.1063/1.5012844
View Table of Contents: http://aip.scitation.org/toc/jcp/148/8
Published by the American Institute of Physics

Absolute cross section measurements for the scattering of low- and intermediate-energy electrons from PF_3. II. Inelastic scattering of vibrational and electronic excitations

N. Hishiyama,[1] M. Hoshino,[1,a)] F. Blanco,[2] G. García,[3] and H. Tanaka[1]
[1]*Department of Physics, Sophia University, Chiyoda-ku, Tokyo 102-8554, Japan*
[2]*Departamento de Fisica, Atomica, Molecular y Nuclear, Facultad de Ciencias Fisicas, Universidad Complutense de Madrid, E-28040 Madrid, Spain*
[3]*Instituto de Fisica Fundamental, Consejo Superior de Investigaciones Científicas, 28006 Madrid, Spain*

(Received 8 November 2017; accepted 12 February 2018; published online 28 February 2018)

As a sequel paper to our study of the elastic scattering for electron collisions with phosphorus trifluoride, PF_3 molecules, we report absolute inelastic differential and integral cross sections (DCS and ICS) of vibrational excitations for the compound fundamental vibrational modes ν_{13} ($\nu_1 + \nu_3$), ν_{24} ($\nu_2 + \nu_4$), and their sum in the impact energy range of 2.0–10 eV and over a scattering angle range of 20°–130°. The measured angular distributions of scattered electron intensities for the present inelastic scattering are normalized to the elastic peak intensity corresponding to the DCSs of He. These vibrational excitation measurements demonstrate the presence of resonances around 2 eV and also around 6–10 eV. In addition, a generalized oscillator strength analysis is applied to derive oscillator strength f_0-values and (unscaled Born) ICSs from the corresponding DCSs measured for the low-lying optically allowed $8a_1^{-1} \rightarrow 7e\ (\sigma^*)$ excitation band, which is assigned as the Jahn-Teller splitting and $8a_1^{-1} \rightarrow 4s$ Rydberg transition at impact energies of 100, 200, and 300 eV, over a scattering angle range of 1.0°–15°. The f_0-values obtained in the present study are compared with the results of previous photoabsorption and pseudo-optical measurements. The unscaled Born ICSs are compared with the binary-encounter f-scaled Born ICSs estimated over a wide impact energy region from the excitation thresholds. *Published by AIP Publishing.* https://doi.org/10.1063/1.5012844

I. INTRODUCTION

A literature survey of previous experimental and theoretical studies on low- and intermediate-energy electron scattering from PF_3 was presented in Paper I[1] (hereafter, Ref. 1). As mentioned therein, prior experimental studies were restricted to the formation of positive and negative ions,[2–4] total cross section (TCS) measurements,[5] and absolute photoabsorption oscillator strength determinations for valence and inner shells.[6] From the practical point of view, most of the electron-impact excitation cross section data needed for modeling plasma processes are still not available in the literature. The lack of reliable inelastic cross section values prevents progress toward a more thorough understanding of the relevant phenomena.

In this paper, we present absolute vibrational excitation differential cross sections (DCSs) for the composed fundamental vibrational modes ν_{13} ($\nu_1 + \nu_3$) and ν_{24} ($\nu_2 + \nu_4$) at impact electron energies below 10 eV, for scattering angles from 20° to 130°. These vibrational excitation DCS measurements, when coupled with the elastic angular distribution, allow the identification of several resonances which are compared with those predicted by the R-matrix calculation of Ref. 7. Furthermore, absolute inelastic cross sections for the low-lying optically allowed $8a_1^{-1} \rightarrow 7e\ (\sigma^*)$ excitation band, assigned as the Jahn-Teller splitting, and $8a_1^{-1} \rightarrow 4s$ Rydberg transitions,[6] were measured at impact energies of 100, 200, and 300 eV for scattering angles ranging from 1.0° to 15°. From these results, along with a generalized oscillator strength (GOS) analysis, we derived the oscillator strength f_0-values and the binary-encounter-f (BEf)-scaled ICSs[8] over a wide energy region, from the excitation threshold to 5000 eV. Finally, we estimate our experimental total cross sections below 10 eV by adding the sum of the vibrational inelastic cross sections ($\nu_1 + \nu_2 + \nu_3 + \nu_4$) to the elastic ICS[1] and compare the present electronic excitation cross sections with the total inelastic ICS calculated by the independent atom model with the screening corrected additivity rule (IAM-SCAR) method above the threshold. Here, the fundamental vibrational modes, ν_1, ν_2, ν_3, and ν_4, correspond to symmetric stretching (110.6 meV), symmetric deformation (60.4 meV), degenerated stretching (106.6 meV), and degenerated deformation (42.7 meV), respectively.[9]

In Sec. II, we briefly describe the experimental system and procedures used to carry out the present measurements. In Sec. III, we present a brief report on the calculation and extrapolation methods applied to the experimental DCS values to derive the corresponding integral cross sections. In Sec. IV, the experimental data for inelastic scattering of vibrational and electronic excitations are presented together with a discussion and compared with other previous studies available in the literature. Finally, some conclusions that can be drawn from the present study are given in Sec. V.

a)Author to whom correspondence should be addressed: masami-h@sophia.ac.jp. Tel.: (+81) 3 3238 4227. Fax: (+81) 3 3238 3341.

II. EXPERIMENTAL DETAILS

The experimental setup and procedure have been described in detail in Ref. 1. For the inelastic electron collision measurements, the original high-resolution spectrometer consisting of a hemispherical monochromator and a similar analyser, computer-controlled lens voltages, and differential pumping have been used. The overall resolution was 40–45 meV (FWHM), as derived from the width of the elastic peak [see Figs. 1(a) and 1(b)], and the current intensity in the target region was typically 3–6 nA, depending on the impact energy. The nozzle was kept at slightly elevated temperatures (50 °C–70 °C) throughout the measurement, which—at this resolution—will not lead to appreciable rotational broadening because of the small rotational constants of PF_3, i.e., $\sim 6.4 \times 10^{-5}$ eV ($J = 0 \rightarrow 1$).[7] Even the much lighter N_2 requires a resolution of ~10 meV in order to reveal a broad rotational structure in energy-loss measurements in beam-beam experiments.[10,11] Similarly, no rotational broadening of the elastic peak could be observed in the present measurements. At a temperature of 70 °C, the lower fundamental vibrational modes of PF_3 beginning with ν_4 (42.7 meV), ν_2 (60.4 meV), ν_3 (106.6 meV), and ν_1 (110.6 meV)[9] can be excited together with rotational excitations, which would contribute slightly to the elastic peak, resulting in the superelastic peak which can be seen in Figs. 1(a) and 1(b). With the present energy resolution, these cannot be resolved, and thus in the present analysis of the vibrational excitation, we use the deconvolution procedures described below. Note that two modes ν_3 (106.6 meV) and ν_1 (110.6 meV) are very close and thus treated as one mode ν_{13} in the present analysis. The incident electron energy was calibrated against the ^2S Feshbach resonance of He at 19.37 eV.

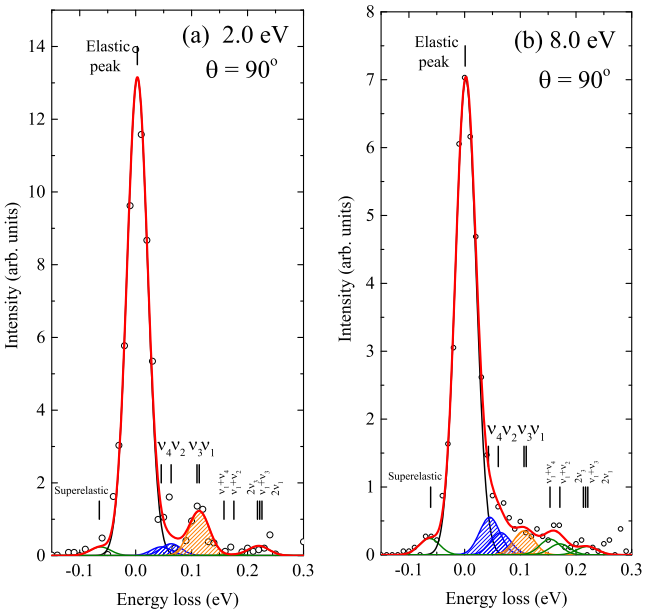

FIG. 1. Typical energy loss spectra of scattered electrons from PF_3 at impact energies of (a) 2.0 eV and (b) 8.0 eV, at a scattering angle of 90°, with an energy-resolution of ~40 meV. The energy positions of the elastic peak, low-lying fundamental vibrational modes, their overtones and combinations, and a superelastic peak from the vibrational deexcitation are shown in the bar plots.

The experimental study was divided into two regimes: (a) vibrational excitations of the composed fundamental vibrational modes ν_{13} ($\nu_1 + \nu_3$), ν_{24} ($\nu_2 + \nu_4$), and their sum at fixed incident electron energies, E_0 = 2.0, 3.0, 4.0, 6.0, 8.0, and 10 eV and scattering angles ranging from 20° to 130° (see Fig. 1), and (b) electronic excitations, in the energy loss (ΔE) range 7.5 eV ≤ ΔE ≤ 11.5 eV, at impact energies of 100, 200, and 300 eV and scattering angles ranging from 1.0° to 15° (see Fig. 2). Note that the transmission efficiency of the analyzer[12] has been calibrated with the same procedures for both the vibrational and electronic excitation measurements, leading to considerably small correction factors, and an efficiency of ~1.0 over the whole energy range considered here, because the ratio of ΔE to E_0 varies roughly in the narrow range of $0.015 < \Delta E/E_0 < 0.100$ for the vibrational excitation and $0.025 < \Delta E/E_0 < 0.115$ for the electronic excitation, respectively.

In this study, the relative intensities of scattered electrons corresponding to vibrational excitations have been converted into absolute cross section values by using the well-established relative flow technique[13–16] to normalize them to the standard elastic DCS of He,[17] whereas those corresponding to electronic excitations at higher impact energies, above 100 eV, and forward scattering angles smaller than 10°, have been normalized to the benchmarked inelastic DCSs of the He $1s^2\ ^1S \rightarrow 1s2p\ 2^1P$ transition.[18,19] These normalization procedures require the constant Knudsen numbers of PF_3 and He to generate two equal gas densities in the collision volume. This condition was achieved when the head pressures behind the nozzle were 0.6 Torr for PF_3 and 1.8 Torr for He, for molecular diameters which were estimated using the hard sphere model (3.8 Å and 2.18 Å, respectively; see Ref. 1 for details).

Uncertainty limits connected with the present experimental data are estimated as follows; the He reference data used to normalize the relative electron scattering intensities are accurate to within 10%. The electron detection system introduces another ~3%–10% as statistical uncertainties, and the DCS extrapolation procedure to obtain the inelastic ICSs (see Sec. III) contributes an additional ~15%. For the vibrational

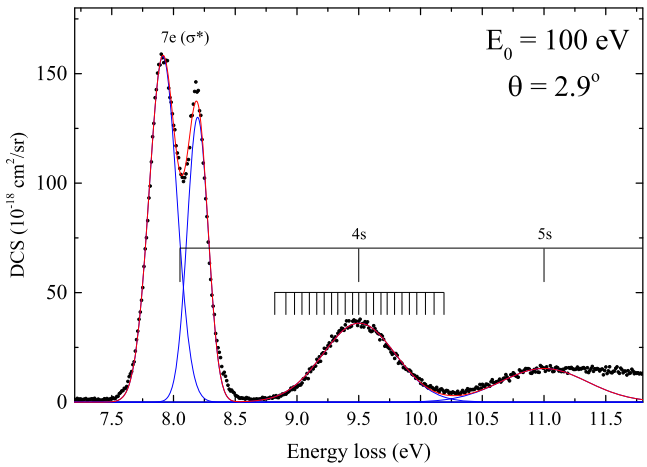

FIG. 2. A typical electron energy loss spectrum of PF_3 in the energy loss range 7.3–11.8 eV at an impact energy of 100 eV and a scattering angle of 2.9°. Red and blue lines represent the total and the individual fitting results.

excitations, the deconvolution procedure using Gaussian profiles (see Sec. III A) introduces uncertainties of a further ~15%–20%. By combining these partial error sources, the total uncertainty limits of the present cross section values are estimated to be within ~28% for the vibrational DCSs, ~32% for the vibrational ICSs, ~20% for the electronic excitation DCSs, and ~28% for the electronic excitation ICSs. Note that these values are consistent with those estimated for the elastic cross sections in Ref. 1.

III. DATA ANALYSIS AND BE*f*-SCALING

A. Peak deconvolution procedures

As shown in Figs. 1(a) and 1(b) (see also Fig. 1 of Ref. 1), spectral deconvolution procedures enable the separation of the elastic peak from those corresponding to vibrational excitations. With the present energy resolution of 40–45 meV, the tail of the elastic peak overlaps the lowest-lying vibrational excitation peak. Before deconvolution, this longer tail, lying on the energy-loss side of the elastic peak, was subtracted using the similar tail corresponding to the elastic peak of He. Gaussian profiles were assumed for all the observed peaks which were assigned to elastic scattering, the three fundamental vibrational modes (ν_{13}, ν_2, and ν_4), their overtones, and their combinations, as shown in Figs. 1(a) and 1(b). For each impact energy, single DCS components were extracted from the measured electron energy spectra by using a standard spectral deconvolution procedure.[20] In the present analysis, the superelastic peak from vibrational deexcitations at an energy loss of ~−63 meV was considered as a single Gaussian peak.

Furthermore, electronic excitation cross sections were derived for the two intense optically allowed transitions shown in Fig. 2. This figure represents a typical electron energy loss (EEL) spectrum of PF_3 at 100 eV impact energy and scattering angle of 2.9° recorded with an energy resolution of ~40 meV. As shown in Fig. 2, the first double peak, in the 7.4–8.6 eV ΔE range fitted by two Gaussian functions, corresponds to the $8a_1{}^{-1} \rightarrow 7e\,(\sigma^*)$ transition band, which is split due to the Jahn-Teller effect.[6] The next energy loss feature, from 8.6 to 10.3 eV, has been fitted by a single Gaussian function and represents the broad band with 24 vibrational progressions corresponding to the $8a_1{}^{-1} \rightarrow$ 4s Rydberg and/or $9a_1$ virtual valence excitations. Note that the present energy resolution (~40 meV), together with statistical fluctuations, do not allow us to resolve the fine vibrational structure for this $4s/9a_1$ transition. Note that the excitation cross sections for only two optically allowed transitions to 7e (σ^*) and $4s/9a_1$ were obtained in the present study because the 5s broad band was structureless and continuum-like, as shown in Fig. 2.

B. Fitting and integrating procedure for vibrational excitations

To obtain the experimental vibrational excitation ICSs, the present measured DCSs were extrapolated to the scattering angle regions not experimentally accessible, i.e., $\theta < 10°$ and $130° < \theta$, by means of the modified phase shift analysis (MPSA) procedure.[21] Numerical integrations of the DCSs from 0° to 180° yield the ICS as follows:

$$\mathrm{ICS} = 2\pi \int_0^{\pi} \mathrm{DCS} \sin\theta d\theta. \tag{1}$$

The MPSA fitting applied to the vibrational excitation DCSs was not corrected to account for dipole-Born interactions, which mainly affect the forward scattering amplitudes because of negligibly small infrared absorption intensity obtained from IR spectra and a quantum chemical calculation.[22] It should be noted again that the vibrational excitation cross sections measured with the present energy resolution include rotational excitations (and deexcitation). As mentioned before, we experimentally obtained differential and integral elastic[1] and vibrational excitation cross sections in the present study, while other data presented in this paper have been theoretically obtained. These include differential elastic as well as integral elastic and inelastic (electronic excitation plus ionization) cross sections together with differential and integral dipole-Born rotational excitation cross sections. In addition, ICSs for two intense optically allowed electronic excitations were separately determined by applying a generalized oscillator strength analysis (see Sec. III C).

C. Generalized oscillator strength analysis for optically allowed electronic excitations

Electronic excitation ICSs have been derived by applying a generalized oscillator strength analysis and then assessed for the optically allowed transitions with the BE*f*-scaling procedure. Briefly, the DCSs for electronic excitations derived from the present measurements were transformed to generalized oscillator strengths (GOSs) as a function of the squared momentum transfer, K^2, by means of the standard formula.[23] The experimental GOSs are least squares fitted using the semi-theoretical formula proposed by Vriens[24] for dipole allowed transitions as follows:

$$\mathrm{GOS}\left(K^2\right) = \frac{1}{(1+x)^6}\left[\sum_{m=0}^{\infty} \frac{f_m x^m}{(1+x)^m}\right], \tag{2}$$

where

$$x = \frac{K^2}{\alpha^2}$$

and

$$\alpha = \sqrt{\frac{B}{\mathrm{R}}} + \sqrt{\frac{B-E}{\mathrm{R}}}.$$

Here, B and E are the binding and excitation energies for the excited target electrons, respectively. R is the Rydberg constant. The f_m values in Eq. (2) are fitting constants determined from a least-squares fitting of the experimental GOSs. The experimental optical oscillator strengths (OOSs) for the optically allowed transitions can be derived from the f_0-coefficient values, which can be determined from the limit of $K^2 \rightarrow 0$, under the assumption that the Born approximation is valid for the considered transition. In general, when the Born approximation for an excitation is satisfied, the GOSs for different impact energies show the same trend, as a function of K^2, with independence of the impact energy. Employing this procedure, the impact energy region satisfying the Born approximation can be determined and the experimental OOS (f-value) can be derived and compared with the experimental value from photoabsorption or pseudo-optical (high energy electron) measurements.

Experimental ICSs as a function of the incident energy, E_0, can be then obtained from the standard formula[23] in the following equations:

$$\mathrm{ICS}\,(E_0) = \frac{4\pi a_0}{E_0/R} \int_{K_{\min}{}^2}^{K_{\max}{}^2} \frac{\mathrm{GOS}\left(K^2\right)}{E/R} d\left(\ln K^2\right) \qquad (3)$$

with

$$K_{\min}{}^2 = \frac{2E_0}{R}\left[1 - \frac{E}{2E_0} - \sqrt{1 - \frac{E}{E_0}}\right] \qquad (4)$$

and

$$K_{\max}{}^2 = \frac{2E_0}{R}\left[1 - \frac{E}{2E_0} + \sqrt{1 - \frac{E}{E_0}}\right]. \qquad (5)$$

Here, $K_{\min}{}^2$ and $K_{\max}{}^2$ are the momentum transfer values which correspond to the scattering angles 0° and 180°, respectively and a_0 is the Bohr radius.

D. BE*f*-scaling

The BE*f*-scaled Born ICS determination method for optically allowed transitions was initially proposed by Kim.[25] In general, the electron impact excitation cross sections for optically allowed transitions calculated with the Born approximation are in fairly good agreement with experimental and more sophisticated theoretical ICSs for relatively high impact energies. The level of agreement becomes poorer as the impact energy decreases toward the threshold excitation energy. Kim hence developed a simple scaling formula to correct the Born electron impact excitation ICS (σ_{Born}) for several atomic targets over the entire energy range[23] and then extended his method to several molecular targets.[26] Briefly, the BE*f*-scaled Born ICS, σ_{BEf}, is given by

$$\sigma_{BEf}\,(E_0) = \frac{E_0}{E_0 + B + E}\frac{f_{accur}}{f_{Born}}\sigma_{Born}\,(E_0)\,, \qquad (6)$$

where f_{accur} is an accurate f-value experimentally obtained from photoabsorption or pseudo-photon measurements or from accurate theoretical calculations, whereas f_{Born} is from the experimental generalized oscillator strength analysis described above or from calculations within the framework of the Born approximation (1st perturbation), and the term $E_0/(E_0 + B + E)$ is the BE*f*-scaling factor as described in Ref. 25. The f-scaling factor, f_{accur}/f_{Born}, has the effect of replacing the wave function used to calculate the Born cross section, $\sigma_{Born}(E_0)$ with a more accurate one. Hence, the BE*f*-scaling corrects the deficiency of the Born approximation at low impact energies, E_0, without losing its well-known validity for higher incident energies. An excellent review of this BE*f*-scaling method has been recently published by Tanaka *et al.*[8]

IV. RESULTS AND DISCUSSION

A. Vibrational excitation

1. *Differential cross sections*

EEL spectra for the considered impact energies and scattering angles have been decomposed into single fundamental vibrational modes with three Gaussian profiles as shown in Figs. 1(a) and 1(b) (see also Fig. 1 of Ref. 1). From these figures and with the present resolution of 35–40 meV, the elastic peak overlaps with the composed ν_{24} ($\nu_4 + \nu_2$) modes but is clearly separated from the ν_{13} ($\nu_1 + \nu_3$) modes. The present vibrational DCSs are shown from 2.0 to 10 eV impact energies and 20°–130° scattering angles in Fig. 3, which include the results for the sum of the two composed modes, i.e., $\nu_{24} + \nu_{13}$ ($\nu_{sum} = \nu_2 + \nu_4 + \nu_1 + \nu_3$). These compound vibrational DCSs and their angular integrated cross sections (ICSs) are tabulated as numerical data in Table I. Typical DCSs as a function of the scattering angle for these ν_{24} and ν_{13} composed vibrational modes as well as their sum, ν_{sum}, for 2.0 and 8.0 eV are shown in Figs. 4(a) and 4(b), respectively. In the present study, experimental data are also fitted and extrapolated to 0° and 180° scattering angles using the MPSA procedure[1] *without* the dipole-Born correction for forward scattering angles because of the negligible contribution that can be expected from the small transition matrix element magnitudes of vibrational excitations obtained from the IR spectra and quantum chemical calculation.[22] From a theoretical and computational point of view,[27] however, the effect of a permanent dipole moment in the target molecule dominates both inelastic scattering and elastic scattering at lower energies, specifically below 1 eV, for forward angles ≤10°. No comparable experimental and theoretical data for the vibrational excitations of the PF_3 molecule by low energy electron impact are available in the literature. Note that the relatively large dipole moment (1.03 D) of PF_3 was used for the extrapolation of the *elastic* DCS to the forward scattering angles.[1] Note that, as described in Paper I,[1] obtaining information on resonances from the elastic scattering cross section was difficult due to the direct

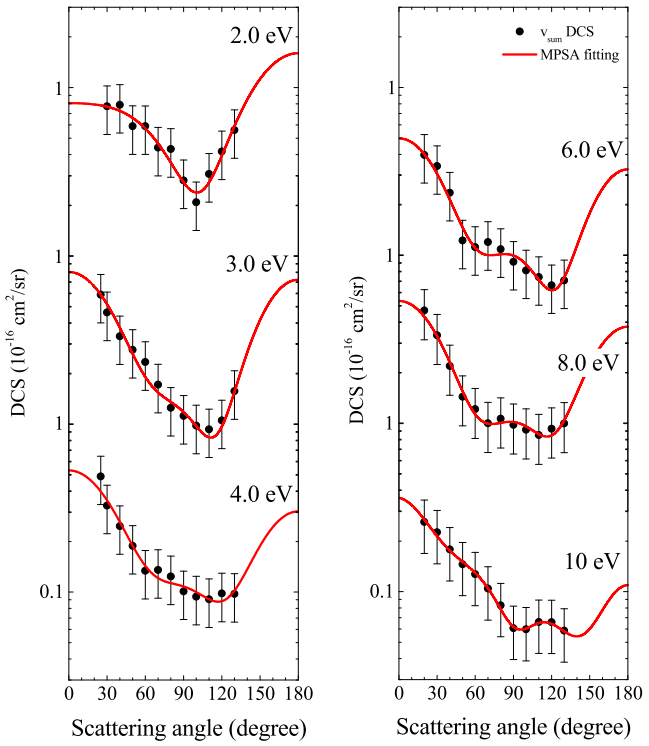

FIG. 3. Sum of the vibrational DCSs for PF_3 in the energy range 2.0–10 eV, together with the present MPSA fitting curves (red).

TABLE I. Compound vibrational differential (10^{-16} cm^2/sr) and integral cross sections, ICS (10^{-16} cm^2) for PF_3. Uncertainties on the DCS are typically ~28%, and on ICS ~32%.

Angle	Impact energy (eV)					
(deg)	2.0	3.0	4.0	6.0	8.0	10
20	...	...	...	0.397	0.466	0.260
25	...	0.591	0.487	0.341	...	...
30	0.774	0.464	0.327	0.237	0.332	0.226
40	0.789	0.334	0.247	0.123	0.219	0.178
50	0.589	0.278	0.188	0.112	0.143	0.146
60	0.589	0.235	0.134	0.120	0.121	0.127
70	0.439	0.172	0.135	0.109	0.100	0.104
80	0.431	0.126	0.124	0.092	0.106	0.083
90	0.281	0.113	0.101	0.092	0.098	0.061
100	0.208	0.099	0.094	0.075	0.091	0.060
110	0.307	0.094	0.091	0.067	0.085	0.066
120	0.417	0.106	0.099	0.071	0.093	0.066
130	0.558	0.158	0.098	0.097	0.100	0.058
ICS	7.12	2.78	2.25	1.77	1.81	1.29

scattering contribution. Fortunately, direct (non-resonant) scattering in vibrational excitation is about a factor of 10 smaller than that in elastic scattering (see Fig. 5 of Ref. 1) and, in general, a resonance is expected to be observed more clearly as enhancements in the vibrational DCS.

The angular undulations of the vibrational DCSs between 2.0 and 10 eV seem to change continuously as a function of the scattering angle, like in the direct (non-resonant) electron-impact vibrational excitation DCSs. In more detail, for low impact energies (between 2.0 and 3.0 eV), however, the angular distributions of the vibrational DCS give appreciably a single minimum near 90°–100°, which show a typical resonant characteristic feature dominated clearly by the p-partial wave. The overall angular distribution represents a similar shape to that for the elastic DCS[1] at 2.0 eV [as shown in Fig. 4(a)]. Further, as the contribution from the d-wave becomes apparent towards higher impact energies, around 8.0 eV, the interference between the two (p and d) waves may rather modify the angular distribution; this minimum gets broader from 60° to 130°, and a small local maximum appears around 90°. This indicates that a weak d-wave shape resonance alters the general characteristics of the direct (non-resonant) vibrational excitation. At 10 eV, however, the angular distribution resembles that for the elastic scattering in exhibiting no distinct resonance behavior showing a broad minimum around 90° with weak structure near 130°.

In a recent R-matrix calculation,[7] two resonances were predicted in the ICS of "the elastic scattering": a shape resonance (2A″) at 0.77 eV and a Feshbach resonance (2A′) at 13.57 eV, respectively.[7] These resonant structures are in good agreement with a broad maximum at about 1 eV and another weak structure between 6 and 15 eV observed in the experimental TCS[5] (see Fig. 6). Furthermore, various peaks or structures have been predicted in the momentum transfer cross section (MTCS) which, in general, provides information about the backward scattering (see Fig. 6). In order to make more visible the structures of the MTCS curve,[7] an inset expanding the scale of Fig. 5 in Ref. 1 from 8 to 15 eV is also shown in Fig. 6. Some of these structures were interpreted corresponding to the formation of negative and positive ions,[3] as indicated by the arrows in the inset of Fig. 6.

2. Example of color scaled two-dimension plot

The vibrational DCS features, considered from a different mapping of the DCSs, can be much more clearly visualized in the color scaled two-dimensional (2D) plot shown in Fig. 5, i.e., a pseudo three-dimensional plot of the vibrational DCS as a function of impact energy and scattering angle. The magnitude of the vibrational DCS is shown in Fig. 5 by color density on a logarithmic scale according to the color bar shown on the right side of the figure. Vertical lines, for a fixed scattering angle, represent the vibrational excitation function of the DCSs. Usually, shape resonances in molecules can be seen in such 2D plots as island-like structures, easily identified by color contrasts. Note that the vibrational excitation functions represented in Fig. 5 are derived from a polynomial fitting to smooth the limited experimental data points. The two resonances theoretically proposed using the R-matrix code[7] at 0.77 eV and 13.57 eV are not covered by this study (2.0–10 eV).

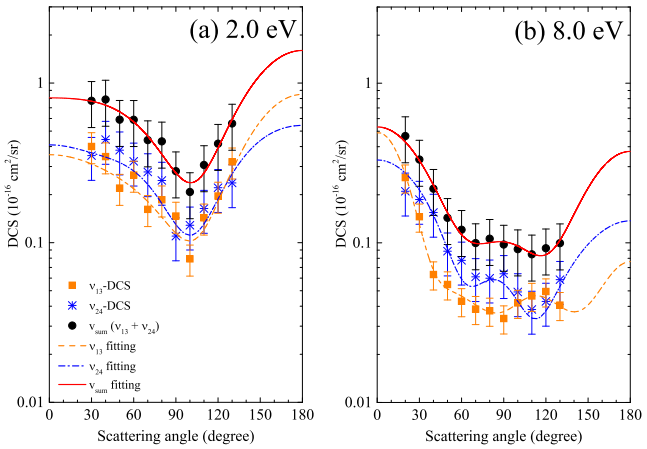

FIG. 4. Typical compound vibrational modes, ν_{13}, ν_{24}, and ν_{sum} DCSs for PF_3 at (a) 2.0 eV and (b) 8.0 eV, together with the MPSA fitting curves (see text for details).

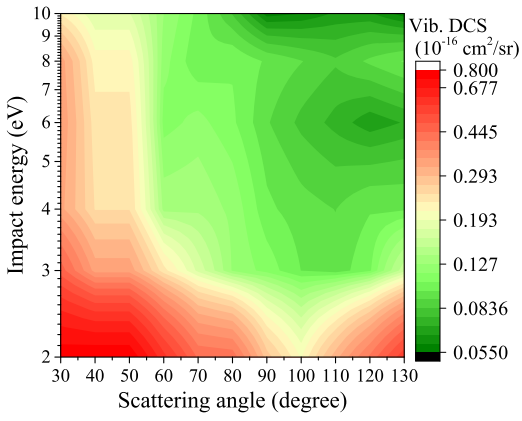

FIG. 5. Two-dimensional plot (pseudo-three-dimensional plot) of the compound vibrational DCS as functions of impact energy and scattering angle. The contrasting density corresponds to the magnitude of the vibrational DCS (logarithm plot).

However, the vibrational excitation function at fixed scattering angle is clearly enhanced as a broad band, which can be identified by color contrast in Fig. 5, between 2.0 and 3.0 eV exhibiting a sharp dip at around 100° for the compound vibrational modes, which corresponds to a p-wave shape in the vibrational DCS at 2.0 eV. Due to the broad nature of the shape resonance, this enhancement feature around 2 eV can be considered to survive in the tail of the shape resonance theoretically predicted at around 0.77 eV impact energy.[7] Furthermore, the faint bump slightly enhanced around 8 eV in the vibrational ICS (see Fig. 6) may correspond to the ridge in the color contrast which extends horizontally as a weak band in the 2D plot of Fig. 5. As discussed below, those two aspects correspond to a resonant-like increasing trend toward a broad maximum around 1 eV and to a very weak bump around 6.0–20 eV in the elastic ICS,[1] MTCS, and the total cross section (TCS) measured by Szmytkowski *et al.*[5] It is noteworthy that from Fig. 5 in Ref. 1 and Fig. 6 in the present study, both features can be interpreted on the basis of two *shape* resonances located in the energy ranges ~1–3 eV, and ~6–10 eV. Above 10 eV, resonant dissociative electron attachment processes (see Fig. 6) are included in the faint bump extending up to 20 eV in the elastic ICS, MTCS, and TCS, and one of these has been ascribed presumably to the Feshbach resonance predicted theoretically to lie at 13.57 eV,[7] as described below.

3. Symmetry analysis

a. Preliminaries. Further information on the resonances in the vibrational excitation cross sections can be obtained by considering the lowest unoccupied molecular orbitals (LUMO) (virtual orbitals) and a subsequent symmetry analysis based on angular correlation theory.[28,29] Shape resonances often reveal strong selectivity of the vibrational excitation probabilities which strongly depend on the participating partial waves in the scattering process. Note that a shape resonance generally reflects the existence of a compound state consisting of a molecule in the ground state plus an incident electron temporarily trapped in a low-lying unoccupied orbital (a temporary negative ion, TNI). As will be seen in Sec. IV B 3, PF_3 has $^1A_1$ symmetry in the ground state, and the lowest unoccupied molecular orbitals (LUMO), LUMO+1 and LUMO+2 are 7e and $9a_1$, and $10a_1$, respectively,[6] in which the two lowest "optically allowed" TNI states belong to the ^2E and $^2A_1$ representations of the C_{3v} group. Note that the mean-excitation energies of the two lowest excited states correspond to the transitions observed experimentally at 8.06 eV and 9.5 eV shown in Fig. 2, respectively. The formed TNI states belong to the ^2E and $^2A_1$ representations of the C_{3v} group, and the modes into which these decay are given by the symmetric product $(e \times e) = [\nu_3\ (e), \nu_4\ (e)]$, $[\nu_1(a_1), \nu_2(a_1), \nu_0\ (a_1)]$, and $(a_1 \times a_1) = [\nu_1(a_1), \nu_2\ (a_1), \nu_0\ (a_1)]$, where $\nu_0\ (a_1)$ is the elastic channel. These calculations are summarized in Table II, which also includes the ℓ_{out} values for the outgoing wave in body frame coordinates that belong to $\Gamma_{\text{wave-out}}$. Case A1 and E arise from the inclusion of the two lowest virtual orbitals of a_1 and e, while cases E1 and E2 distinguish different possibilities of the outcome, i.e., the final vibrational state of the molecule (classified into either stretching or deformation modes). For more details, refer to our previous paper on NF_3,[20] another molecule with C_{3v}.

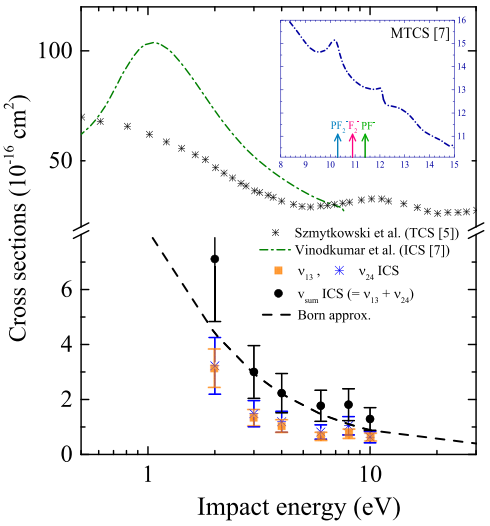

FIG. 6. Vibrational ICSs for the ν_{13}, ν_{24}, and ν_{sum} compound modes obtained from integrating using the MPSA fitting for the vibrational DCSs, together with the prediction of the Born approximation.[1] The experimental[5] and theoretical[7] TCSs, and theoretically calculated momentum transfer cross section (MTCS)[7] are also shown for comparison. The arrows in the small panel represent the impact energies for negative ion formation: PF_2^- (10.3 eV), F_2^- (10.9 eV), and PF^- (11.4 eV).

b. The first shape resonance region around 2 eV. The deconvolution of the EEL spectrum at 2.0 eV incident energy shows the presence of ν_2, ν_4, and ν_{13} even for scattering angles as large as 90° [see Fig. 1(a)] and 130° (see Fig. 1 of Ref. 1). In particular, the contributions of ν_2 and ν_{13} are large within the fitting uncertainties, and the harmonics seem to contain overtones of these. According to Table II, without needing to recur to overlapping vibrational modes, the clear presence of four fundamental modes in the ν_{24} and ν_{13} compound peaks and in their overtones indicates that the trapping orbital must be of the *e* symmetry species. Another confirmation of these results is suggested in Table II, in which the angular momenta ℓ_{out} are presented for the outgoing electron wave in body frame coordinates. We now assume that a close inspection of Fig. 4(a) can approximately locate the maxima and minima in the DCS angular distribution corresponding to the observed feature and thereby identify the low-order Legendre polynomials P_k needed to describe that angular distribution behavior. For the 2.0 eV DCS, the angular distributions of ν_{24} and ν_{13} in the laboratory frame show the behavior of a Legendre polynomial $P_1\ (\theta)$. If the observed DCSs are due to the ^2E resonance, the allowed values of ℓ_{out} in the body frame can be either

TABLE II. Symmetry analysis according to point group C_{3v}.[18]

Species	Case E1	Case E2	Case A1
Ground state	A_1	A_1	A_1
Γ_{TNI}	e	e	a_1
Γ_{final}	a_1	e	a_1
ν	ν_0, ν_1, ν_2	ν_3, ν_4	ν_0, ν_1, ν_2
$\Gamma_{\text{wave-out}}$	e	a_1, e	a_1
ℓ_{out}	1, 2	0, 1, 2	0, 1

$\ell_{out} = 1$ or $\ell_{out} = 2$ [cf. Eq. (7) in Ref. 29]. The former clearly characterizes the p-wave nature in both ν_{24} and ν_{13} so that here again the resonance that fulfils these conditions is the ^{2}E representation (case E1) in Table II. This also confirms the observation of a p-wave feature enhancing resonantly the elastic scattering (ν_0) DCS around 2.0 eV, although it is overlapped with a similar angular distribution from the atomic-like behavior of the central P atom (see Ref. 1).

c. The second shape resonance region around 8 eV. As shown in Fig. 1(b), the deconvolution of the EEL spectrum at 8.0 eV shows again typical resonant enhancements of ν_2, ν_4, ν_{13}, and those combinations for a large scattering angle of 90° which needs ν_2 and ν_4 fundamental modes for a good fit. According to Table II, as shown in the case of the 2.0 eV DCSs, this feature can also be ascribed to the ^{2}E resonance (case E2), in which the TNI decays preferentially into ν_3 (e) and ν_4 (e). This is confirmed by the resonant characteristics in their observed angular distributions as shown in Fig. 4(b), which clearly depend on the TNI decay channels into the ν_{13}, ν_{24}, and ν_0 final vibrational states, respectively, via the ^{2}E resonance. For ν_{24}, a quick inspection reveals a broad structure centered at 90°, with two minima at 60° and 120° scattering angles, so that a description of the angular distribution requires Legendre polynomials of $P_2(\theta)$. Consequently, we obtain ℓ_{out} = 0, 1, and 2 for the scattered electron angular momentum in body-frame coordinates, which corresponds to case E2 in Table II. Therefore, the resonance around 8 eV can only be detectable in the vibrational excitation channel, not predicted theoretically in elastic scattering.[7] In short, the angular distributions of the vibrational DCSs observed at 2.0 and 8.0 eV are consistent with the symmetry analysis of Table II and can both be attributed to an "e-symmetry resonance" connected with the assumed LUMO (for the "optically allowed" state) at 8.06 eV in Fig. 2.

4. Vibrational excitation ICS

Figure 6 shows vibrational ICSs for the compound modes ν_{13}, ν_{24}, and ν_{sum} obtained from the above-mentioned experimental DCS integration procedure using the MPSA fitting and the calculation using the Born approximation[30] for the direct (non-resonant) vibrational excitation. As predicted from the dipole-Born approximation, the ICSs for direct-impact vibrational excitation of molecular vibration decrease smoothly with impact energy ($\propto 1/E_0$) for the energy range considered in the present study (see the dashed line in Fig. 6). However, our experimental vibrational ICSs for the compound modes of ν_{13} and ν_{24} deviate clearly from this curve, showing distinctly "a steep ascent" toward a broad maximum around 1 eV and "a very weak bump" around 6–10 eV, as previously observed for the elastic ICS, the TCS, and the MTCS[7] (see also Fig. 5 of Ref. 1). The behavior of the vibrational excitation cross section in the resonance region depends critically on the lifetime of the TNI. Resonances with lifetimes which are short compared to the vibrational period result in broad (few electron volts) resonances and, therefore, in enhancements of the cross sections observed as two shape resonance regions around 2 and ~6–8 eV in the present vibrational ICS.

The R-matrix calculation of Vinodkumar *et al.*[7] predicted three low-lying excited states (3A″, 3A′, and 1A″). Their excitation ICS results for the first two states showed that the characteristic energy dependence of "optically forbidden" transitions at the excitation threshold was appropriate to excite the lowest "triplet" state. Presumably, the ~2 eV resonance may be ascribed to a TNI associated with the lowest triplet state belonging to e-symmetry, i.e., to the 3A″ state. Following this analysis, the resonant feature at ~8 eV can tentatively be assigned to a TNI connected with the lowest optically allowed state. Here, we note that the theoretical assignments of the intermediate 2A″ and 2A′ resonances differ from the present resonances because of the three lowest C_s symmetry electronic excited states (3A″, 3A′, and 1A″) employed in the R-matrix code.[7] In any case, further "*ab initio*" level calculations for this molecular system are still desirable, before any definitive classification of these resonances is made.

In addition, as mentioned above, the weak maximum observed around 6–20 eV in the elastic ICS,[1] the MTCS, and the measured TCS[5] may be influenced by another resonance, such as the Feshbach resonance at 13.57 eV, belonging to the A_1 representation with the incident electron trapped in the a_1 orbital, as predicted theoretically.[7] This would indicate that the partial wave involved in this small local minimum was slightly influenced again by a p-wave contribution to the elastic DCS.[1] However, no resonant enhancement (feature) is observed around 10 eV in the vibrational DCS and ICS, as shown in Figs. 5 and 6.

Further information on the TNI (PF_3^{*-}) is usually obtained through dissociative electron attachment[2–4] with the metastable parent anion decaying resonantly into negative ions such as PF_2^-, F_2^-, and PF^- at 10.3, 10.9, and 11.4 eV, respectively, as shown in Fig. 6. These results may imply that the potential surface of the TNI states from a parent PF_3^- ion represents a dissociative antibonding shape resonance of a_1 (P–F σ^*) character, leading to the excitation of the P–F symmetric stretching vibrational mode, and that the dissociation of the parent negative ion occurs much faster than the auto-detachment of the shape resonance. The identified weak maxima in the elastic ICS, the TCS, and the MTCS can be attributed partially to these short-lived shape resonances weakly competing with the dissociative electron attachment processes. However, as discussed in Ref. 1, it is also clear that contributions from electronic excitations and ionization dominate the inelastic scattering processes in the second resonant region. Note that the ^{2}E resonance, visible in the vibrational excitation channel around 2.0 eV and 8.0 eV, apparently does not lead to the production of negative ions.

Finally, it is interesting to note that continuum MS-Xα calculations[31] predicted two resonances, in the a_1 continuum channel at 3 eV, and the overlapping a_1 and e continuum channels at around 10 eV. This calculated result was consistent with the structures experimentally observed in the P 2p and F 1s inner-shell photoionization cross sections as a function of photon energy.[31] However, the order of the resonant states assigned from the lowest virtual orbitals in the present study is inverted in this interpretation[31] [a_1 (F 1s), e (P 2p) were employed, while 7e, 9a_1 are used in the present case].

B. Electronic excitations

Figure 2 shows a typical EEL spectrum at 100 eV and 2.9° scattering angle. Figure 7 illustrates the generalized oscillator strengths (GOSs) as a function of momentum transfer squared for the $8a_1^{-1} \rightarrow 7e\ (\sigma^*)$ and $8a_1^{-1} \rightarrow 4s$ excitations,[6] together with the fitting curves of Vriens.[24] Experimental ICS and BE*f*-scaled Born ICS, σ_{BEf}, as well as plane Born ICS, σ_{Born}, for these transitions are shown in Fig. 8. The corresponding optical oscillator strengths obtained from the present GOS analysis shown in Sec. III C are summarized in Table III.

1. Electron energy loss spectrum

The PF_3 molecule, which belongs to the C_{3v} symmetry group with trigonal pyramidal geometry, has a ground state ($^1A_1$) electronic configuration given by[3]

$$(P1s)^2(F1s)^6(P2s)^2(P2p)^6(5a1)^2(3e)^4(6a1)^2(4e)^4(7a1)^2(5e)^4(1a2)^2(6e)^4(8a1)^2(7e)^0(9a1)^0(10a1)^0.$$

Here, the configurations $(P1s)^2(F1s)^6(P2s)^2(P2p)^6$ and $(5a_1)^2(3e)^4$ represent the inner shells and inner valence shells, whereas $(6a_1)^2(4e)^4(7a_1)^2(5e)^4(1a_2)^2(6e)^4(8a_1)^2$ and $(7e)^0(9a_1)^0(10a_1)^0$ correspond to the outer valence shells of the ground electronic state and the virtual excited state orbitals, respectively.[6] Figure 2 shows a typical experimental EEL spectrum of PF_3 recorded at 100 eV impact energy and 2.9° scattering angle with ~40 meV (full width at half maximum) energy resolution. The first peaks in the EEL range from 7.4 to 8.6 eV have been assigned as the $8a_1^{-1} \rightarrow 7e\ (\sigma^*)$, which presents band splitting due to the Jahn-Teller effect. The second peak in the 8.6–10.3 eV range has been attributed to both the 4s Rydberg and $9a_1$ virtual valence transitions with 24 vibrational progressions.[6] However, due to statistical and energy resolution limitations, we have analyzed this structure as a broad Gaussian peak without vibrational structure. Note that the very weak intensities of the vibrational progressions are observed both in the present measurements and in previous pseudo-optical (high energy electron) spectroscopy[6] and photoabsorption measurements.[32] In this study, we assign the first doublet peaks for the C_{3v} molecule as arising from the Jahn-Teller distortion, via vibronic coupling. We then assume that, due to the Jahn-Teller distortion, a nonlinear molecule such as PF_3 which has a degenerate electronic state can mix states of lower symmetry to the C_s group and remove the degeneracy. As mentioned above, in fact, the R-matrix calculations from Ref. 7 were performed for the C_s group symmetry, including the three lowest electronic excited states, 3A′′, 3A′, and 1A′′, and all possible single and double excitations to virtual orbitals.[7]

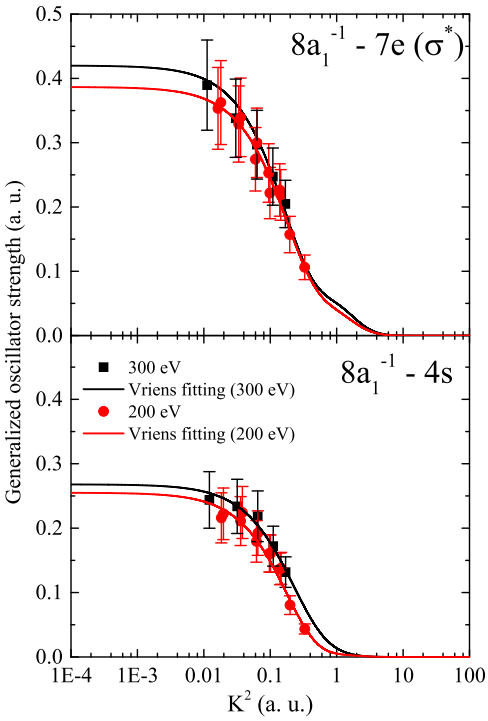

FIG. 7. Generalized oscillator strengths as a function of K^2 for the $8a_1^{-1} \rightarrow 7e\ (\sigma^*)$ transition in the energy loss range 7.4–8.6 eV, and $8a_1^{-1} \rightarrow 4s$ over 8.6–10.3 eV from PF_3 at impact energies of 200 and 300 eV. The solid lines show the results of fitting using the Vriens formula.[22]

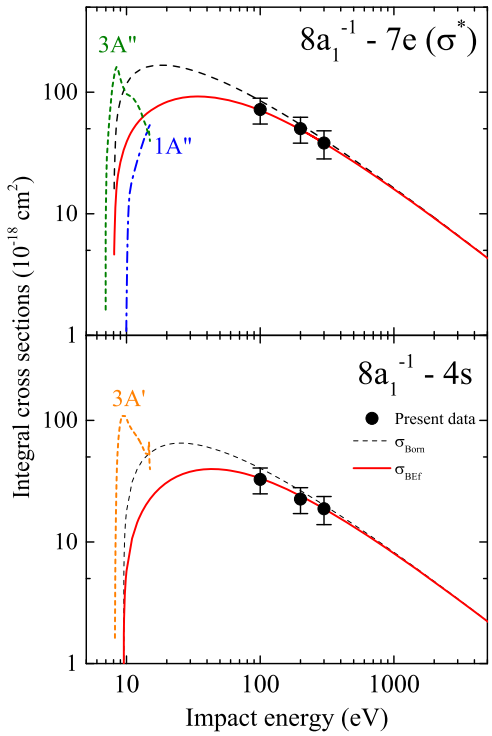

FIG. 8. The excitation ICSs (10^{-18} cm^2) for the $8a_1^{-1} \rightarrow 7e\ (\sigma^*)$ and $8a_1^{-1} \rightarrow 4s$ transitions in PF_3. •: Present excitation ICSs; solid and dashed lines: BE*f*-scaled and Born ICSs, respectively. The calculated results based on the R-matrix code[7] are also plotted in this figure.

TABLE III. A comparison of present OOSs with the available experimental ones for the $8a_1^{-1} \rightarrow 7e\ (\sigma^*)$ and $8a_1^{-1} \rightarrow 4s$ transitions in PF_3.

Authors	7e (σ^*)	4s
Present work	0.41 ± 0.10	0.25 ± 0.07
Au *et al.*[6]	0.4604	0.2542
McAdams and Russell[32]	0.48	0.28

2. Generalized oscillator strength

Figure 6 shows the present GOS results, as a function of K^2, for the $8a_1^{-1} \rightarrow 7e\ (\sigma^*)$ and $8a_1^{-1} \rightarrow 4s^6$ transitions of PF_3 in the EEL ranges of 7.4–8.6 eV and 8.6–10.3 eV and electron impact energies of 200 and 300 eV, respectively. As shown in Fig. 7, the GOSs at 300 eV impact energy are slightly larger than those at 200 eV for both considered transitions. Thus, in this study, we employed the GOSs at the highest impact energy (300 eV), in order to determine the OOSs and the σ_{Born} as described in Sec. III C. For the present fitting procedure, based on the Vriens formula,[24] we used values of B = 11.38 eV,[33] E = 7.91 and 8.18 eV for the $8a_1^{-1} \rightarrow 7e\ (\sigma^*)$, and 9.51 eV for the $8a_1^{-1} \rightarrow 4s$ transitions, respectively, as estimated from our measurements. Note that the intensity of the double peak (caused by the Jahn-Teller effect[6]) which corresponds to the $8a_1^{-1} \rightarrow 7e\ (\sigma^*)$ excitation has been derived from the sum of the intensities of the 7.91 eV and 8.18 eV peaks obtained from the experimental EEL spectrum, as shown in Fig. 2. Table I shows a comparison of the present f_0-values with the experimental OOSs available in the literature. This comparison of our f_0-values, derived from GOS measurements, with the photoabsorption data[32] and pseudo-optical measurements[6] provides an important assessment to verify and validate the present measurements. Our f_0-values for the above transitions are 0.42 (±0.10) and 0.27 (±0.07), which agree reasonably well, within the experimental uncertainties, with the values of 0.48 and 0.28 from the photoabsorption[32] experiments, and 0.46 and 0.25 from the pseudo-optical measurements.[6]

3. BEf-scaled Born ICS

Inelastic ICSs for the $8a_1^{-1} \rightarrow 7e\ (\sigma^*)$ and $8a_1^{-1} \rightarrow 4s$ excitation transitions at impact energies of 100, 200, and 300 eV were obtained by numerical integration of the fitted GOSs over the K^2 limits corresponding to $\theta = 0°$ and 180° in Eqs. (3)–(5). The corresponding results for both transitions are plotted in Fig. 8. In addition, plane wave *apparent* Born ICSs, σ_{Born}, are also plotted in the figure (dashed lines) for comparison. These values have been obtained by extending the σ_{Born} calculations to the lower energy region with the same procedure as that used for the fitted GOS at 300 eV which is illustrated in Fig. 7. For this analysis, we used the unscaled σ_{Born} estimated from the highest-energy experimental results (300 eV) in Eq. (3) because no σ_{Born} calculation was available in the literature. Thus, the f_0-values of 0.42 and 0.27 obtained from our GOS analysis for each transition were employed as the f_{Born} parameters in Eq. (6). As the present f_0-values were in good agreement with the previous experimental studies available in the literature,[6,29] we assumed the factor $f_{accur}/f_{Born} \sim 1$. The BE$f$-scaled ICSs, σ_{BEf}, for each excitation transition derived from the σ_{Born} by Eq. (6) are also plotted in Figs. 6(a) and 6(b). As shown in Fig. 8, for intermediate impact energies the σ_{BEf} generates more reliable values than the unscaled σ_{Born} for the optically allowed $8a_1^{-1} \rightarrow 7e\ (\sigma^*)$ and $8a_1^{-1} \rightarrow 4s^6$ transitions in PF_3. Further experimental and theoretical studies would be needed in order to verify the present σ_{BEf} for lower energies from threshold to 100 eV. At intermediate impact energies, the largest cross sections for electronic excitations are, in general, associated with optically allowed transitions. These cross sections increase gradually in magnitude with increasing impact energies from threshold, reaching a maximum value and then decreasing slowly for higher energies. This behavior agrees with the present energy dependence shown in Fig. 8 for the above transitions in PF_3. The R-matrix electronic excitation cross sections from Ref. 7 are also plotted in Fig. 8. The energy dependence of the excitation cross sections calculated by the R-matrix code[7] partly differs from that of the optically allowed transitions measured in the present measurement. The calculated cross sections assigned to $3A''$ and $3A'$ transitions in Ref. 7 seem to represent typical spin forbidden behavior that readily occurs via electron exchanges, indicated by the steep rise in the ICS near the threshold energy, the maximum value lying a few electron volts above this threshold and the sharp decrease with increasing impact energies. On the other hand, for the calculation assigned to the $1A''$ transition, though the threshold energy is shifted to ~2 eV to the higher energy side with respect to ours, the energy dependence of the calculated cross section reproduces well the present σ_{BEf} for the lowest-lying $8a_1^{-1} \rightarrow 7e\ (\sigma^*)$ transition, increasing gradually as the impact energy increases. Note that in Ref. 7, calculations for the $1A'$ transition corresponding to the 4s Rydberg transition were not reported.

Finally, our experimental ICSs for vibrational and electronic excitation cross sections were compared with the elastic scattering ICS, TCS, MTCS, total inelastic ICS, and ionizations, available in the experimental and theoretical literature in Sec. IV C of Ref. 1. Figure 6 shows that the major contribution to the experimental TCS is from the elastic ICSs for low impact energies. Moreover, as predicted theoretically, rotational excitation of a highly polar molecule, like PF_3, has a significant influence on the TCS especially below 1 eV. Referring to the steep ascent of the vibrational excitation in Fig. 6, the present measurement has not yet reached the broad peak around 1 eV which could be attributed to dipole interaction (the dashed line in Fig. 6) and to shape resonance, but further confirmation requires measurement at much lower impact energies in the region below 1 eV. For higher impact energies, the experimental vibrational excitation cross sections are of the order of 10^{-16} cm^2, decreasing smoothly with a broad weak shape resonance in the energy range from 2.0 to 10 eV. As expected, at intermediate and high impact energies, the electronic excitation and ionization processes represent the major contributions to the TCS.

V. CONCLUSION

In this study, as a sequel to our report on the elastic scattering for electron collisions with phosphorus trifluoride, PF_3

molecules,[1] we report absolute inelastic differential and integral cross sections (DCS and ICS) of vibrational excitations for the compound fundamental vibrational modes ν_{13} ($\nu_1 + \nu_3$), ν_{24} ($\nu_2 + \nu_4$), and their sum in the impact energy range of 2.0–10 eV over a scattering angle range of 20°–130°. The analysis of our present measurements, together with the angular correlation theory to assist with their interpretation, suggests that (a) for vibrational excitations, the resonances observed around 2 eV and 8 eV are both of ^{2}E-symmetry, and (b) for elastic scattering, the weak maximum observed around 10–15 eV can be ascribed to another resonance of the A_1 representation with the incident electron trapped in the a_1 antibonding orbital. The two resonances (around 2 eV and 6–10 eV) are largely consistent with the resonance states of 2A″ (0.77 eV) and 2A′ (13.57 eV) predicted theoretically by the R-matrix code.[7] Nonetheless, a definitive assignment of these resonances awaits a high-quality *ab initio* calculation using, for example, the Schwinger multichannel approach. We have also reported the oscillator strength values, the unscaled Born, and the BE*f*-scaled Born ICSs for the $8a_1^{-1} \rightarrow 7e$ (σ^*) and $8a_1^{-1} \rightarrow 4s$ transitions, where the BE*f*-scaling is effective to reduce the unscaled Born ICS overestimated intrinsically below 100 eV. The present inelastic cross section data for PF_3, together with the elastic scattering results,[1] are expected to be useful for important application fields such as plasma-assisted fabrication based on fluorine compound molecules.

ACKNOWLEDGMENTS

This work was conducted under support of the Ministry of Education, Culture, Sports, Science and Technology-Japan. F.B. and G.G. acknowledge partial financial support from the Spanish Ministerio de Industria, Economia y Competitivided (Project No. FIS 2016-80440).

[1] N. Hishiyama, M. Hoshino, F. Blanco, G. García, and H. Tanaka, J. Chem. Phys. **147**, 224308 (2017).
[2] K. A. G. MacNeil and J. C. J. Thynne, J. Phys. Chem. **74**, 2257 (1970).
[3] P. W. Harland, D. W. H. Rankin, and J. C. J. Thynne, Int. J. Mass Spectrom. Ion Phys. **13**, 395 (1974).
[4] D. F. Torgerson and J. B. Westmore, Can. J. Chem. **53**, 933 (1975).
[5] C. Szmytkowski, M. Piotrowicz, A. Domaracka, L. Klosowski, E. Ptasinska-Denga, and G. Kasperski, J. Chem. Phys. **121**, 1790 (2004).
[6] J. W. Au, G. Cooper, and C. E. Brion, Chem. Phys. **215**, 397 (1997).
[7] M. Vinodkumar, C. Limbachiya, H. Desai, and P. C. Vinodkumar, Phys. Rev. A **89**, 062715 (2014).
[8] H. Tanaka, M. J. Brunger, L. Campbell, H. Kato, M. Hoshino, and A. R. P. Rau, Rev. Mod. Phys. **88**, 025004 (2016).
[9] T. Shimanouchi, *Tables of Molecular Vibrational Frequencies Consolidated Volume I*, National Standard Reference Data Series (National Bureau of Standards, 1972), Vol. 39, p. 17.
[10] S. F. Wong and L. Dubé, Phys. Rev. A **17**, 570 (1978).
[11] H. Tanaka, *Symposium on Electron-Molecule Collisions, Invited Papers* (University of Tokyo, Japan, 1979), p. 31.
[12] M. Matsui, M. Hoshino, H. Kato, F. Ferreira da Silva, P. Limão-Vieira, and H. Tanaka, Eur. Phys. J. D **70**, 77 (2016).
[13] S. K. Srivastava, A. Chutjian, and S. Trajmar, J. Chem. Phys. **63**, 2659 (1975).
[14] R. T. Brinkmann and S. Trajmar, Rev. Sci. Instrum. **14**, 245 (1981).
[15] J. C. Nikel, P. W. Zetner, G. Shen, and S. Trajmar, J. Phys. E: Sci. Instrum. **22**, 730 (1989).
[16] F. Rugamas, D. Roundy, G. Mikaelian, G. Vitug, M. Rudner, J. Shih, D. Smith, J. Segura, and M. A. Khakoo, Meas. Sci. Technol. **11**, 1750 (2000).
[17] L. Boesten and H. Tanaka, At. Data Nucl. DataTables **52**, 25 (1992).
[18] M. Hoshino, H. Kato, D. Suzuki, H. Tanaka, I. Bray, D. V. Fursa, S. J. Buckman, O. Ingólfsson, and M. J. Brunger, Plasma Sci. Technol. **12**, 348 (2010).
[19] M. Hoshino, H. Murai, H. Kato, M. J. Brunger, Y. Itikawa, and H. Tanaka, J. Chem. Phys. **139**, 184301 (2013).
[20] L. Boesten, Y. Tachibana, Y. Nakano, T. Shinohara, H. Tanaka, and M. A. Dillon, J. Phys. B: At., Mol. Opt. Phys. **29**, 5475 (1996).
[21] L. Boesten and H. Tanaka, J. Phys. B: At., Mol. Opt. Phys. **24**, 821 (1991).
[22] N. B. Sari-Zizi, H. Büger, M. Litz, H. Najib, and J. Radtke, J. Mol. Spectrosc. **177**, 46 (1996).
[23] B. H. Bransden and C. J. Joachain, *Physics of Atoms and Molecules* (Longmans, London, 1983).
[24] L. Vriens, Phys. Rev. **160**, 100 (1967).
[25] Y.-K. Kim, Phys. Rev. A **64**, 032713 (2001).
[26] Y.-K. Kim, J. Chem. Phys. **126**, 064305 (2007).
[27] D. W. Norcross and L. A. Collins, Adv. At. Mol. Phys. **18**, 341 (1982).
[28] F. H. Read, J. Phys. B: At., Mol. Opt. Phys. **1**, 892 (1968).
[29] D. Andric and F. H. Read, J. Phys. B: At., Mol. Opt. Phys. **4**, 389 (1971).
[30] Y. Itikawa, Phys. Rev. A **3**, 831 (1971).
[31] I. Powis, Chem. Phys. Lett. **215**, 269 (1993).
[32] M. J. McAdams and B. R. Russell, Chem. Phys. Lett. **18**, 402 (1973).
[33] See http://webbook.nist.gov/chemistry/ for the physical properties of the molecules.